Lab on a Chip

PAPER

View Article Online
View Journal | View Issue

Cite this: *Lab Chip*, 2020, **20**, 1827

A new microfluidic model that allows monitoring of complex vascular structures and cell interactions in a 3D biological matrix†

Christian G. M. van Dijk, [a] Maarten M. Brandt,[b] Nikolaos Poulis,[a] Jonas Anten,[a] Matthijs van der Moolen,[a] Liana Kramer,[a] Erik F. G. A. Homburg,[c] Laura Louzao-Martinez, [a] Jiayi Pei,[a] Merle M. Krebber,[a] Bas W. M. van Balkom,[a] Petra de Graaf, [d] Dirk J. Duncker,[b] Marianne C. Verhaar, [a] Regina Luttge[c] and Caroline Cheng*[ab]

Microfluidic organ-on-a-chip designs are used to mimic human tissues, including the vasculature. Here we present a novel microfluidic device that allows the interaction of endothelial cells (ECs) with pericytes and the extracellular matrix (ECM) in full bio-matrix encased 3D vessel structures (neovessels) that can be subjected to continuous, unidirectional flow and perfusion with circulating immune cells. We designed a polydimethylsiloxane (PDMS) device with a reservoir for a 3D fibrinogen gel with pericytes. Open channels were created for ECs to form a monolayer. Controlled, continuous, and unidirectional flow was introduced *via* a pump system while the design facilitated 3D confocal imaging. In this vessel-on-a-chip system, ECs interact with pericytes to create a human cell derived blood vessel which maintains a perfusable lumen for up to 7 days. Dextran diffusion verified endothelial barrier function while demonstrating the beneficial role of supporting pericytes. Increased permeability after thrombin stimulation showed the capacity of the neovessels to show natural vascular response. Perfusion of neovessels with circulating THP-1 cells demonstrated this system as a valuable platform for assessing interaction between the endothelium and immune cells in response to TNFα. In conclusion: we created a novel vascular microfluidic device that facilitates the fabrication of an array of parallel soft-channel structures in ECM gel that develop into biologically functional neovessels without hard-scaffold support. This model provides a unique tool to conduct live *in vitro* imaging of the human vasculature during perfusion with circulating cells to mimic (disease) environments in a highly systematic but freely configurable manner.

Received 17th January 2020,
Accepted 27th March 2020

DOI: 10.1039/d0lc00059k

rsc.li/loc

Introduction

Current vascular research focuses on the understanding of fundamental and disease-driven processes for therapeutical purposes and regenerative aims. A broad variety of *in vitro* assays are available in the field, with each designed to study a specific aspect of vascular biology.[1] Endothelial barrier homeostasis is vital for vascular performance and is often assessed in *in vitro* setups.[2] Junction proteins such as vascular endothelial cadherin (VE-cadherin) and zonula occludens 1 (ZO-1) facilitate barrier function,[2,3] and are widely studied in multiple settings, including disease-associated inflammation. During inflammation, VE-cadherin junctions are disrupted by leukocytes, thereby increasing barrier permeability[4] and facilitating diapedesis of these circulating cells.[5–7] Leukocyte extravasation during inflammation requires complex interactions between multiple vascular cell types and the surrounding extracellular matrix (ECM), and are mainly assessed *in vitro* in parallel flow chambers, which allow perfusion of circulating cells over a confluent endothelial monolayer with employment of syringe pumps to control the flow hemodynamics.[8,9] These *in vitro* models offer easily accessible, and (sometimes) high throughput solutions for live confocal monitoring. However, although they provide excellent *in vitro* platforms to study basic vascular mechanisms, the high biological and biomechanical

[a] *Department of Nephrology and Hypertension, University Medical Center Utrecht, PO Box 85500, 3584 CX Utrecht, The Netherlands.*
E-mail: K.L.Cheng-2@umcutrecht.nl; Fax: +31 (0) 88 7556283;
Tel: +31 (0) 88 7557329
[b] *Experimental Cardiology, Department of Cardiology, Thorax Center Erasmus University Medical Center, 3000 CA Rotterdam, The Netherlands*
[c] *Department of Mechanical Engineering, Microsystems Group, Materials Technology Institute (MaTe) and, ICMS Institute for Complex Molecular Systems, Eindhoven University of Technology, 5600 MB Eindhoven, The Netherlands*
[d] *Department of Urology, University Medical Center Utrecht, 3584 CX Utrecht, The Netherlands*

† Electronic supplementary information (ESI) available. See DOI: 10.1039/d0lc00059k

complexity of the natural vasculature give rise to many technical challenges that remain to be addressed. For example, perfusable channels may not mimic the natural vessel geometry[10,11] or are not fully 3D ECM encapsulated due to limitations to the mechanical strength of the available (hydro) gels.[12,13] Co-culture of all relevant vascular cell types may also not be possible in certain setups, and lack of *e.g.* mural cells (pericytes and smooth muscle cells) support may hamper native vascular function *in vivo*.[14–16] On the other hand, animal models which do provide the required complex vascular environment, may also be practically and logistically challenging, are less suitable for high throughput screening, and may be limited in human relevance. The development of novel, more improved *in vitro* systems that combine the complexity of the native vasculature and allow direct monitoring of the cells in a physiologically relevant setting would greatly enhance the current insights into vascular and circulating cell behavior in healthy and different disease conditions.

Microfluidic technology that allows controlled pre-fabrication of perfusable micro-channels in the microvascular range could provide a low cost, high through put-based, quantifiable solution that captures the human microenvironment for in depth mechanistic studies.[17] Moreover, human based microfluidic systems have the ability to bridge the gap between non-complex *in vitro* models and complex, non-human *in vivo* techniques. In the last decade, this technology has been widely applied to successfully mimic human tissues, including the vasculature.[18] Some examples of advanced microfluidic "vessel-on-a-chip" systems include the assay presented by Lam *et al.* which consists of a set of polydimethylsiloxane (PDMS) channels from which the largest one functions as a central angiogenesis chamber with endothelial colony-forming-cell derived endothelial cells (ECFC ECs), connected to adjacent stromal cell chambers and channels with oxygen scavenging compounds.[19] Basic PDMS designs often require micro-vessel formation by sprouting (from adjacent chambers) or self-assembly in an ECM environment in the angiogenic chamber. Here, the additional PDMS channels introduce spatial and temporal variants in local oxygen levels to mimic physiological conditions.[19] By adding more relevant cell types, such as astrocytes and epidermal cells to the vascular cells in the angiogenesis chamber or adjacent chambers, the blood brain barrier and the vascularized skin microenvironment could be replicated more accurately in a variety of comparable PDMS channels based microfluidic systems.[20–23] Similar devices have been presented with micro-channels which are partially in contact with 3D ECM gels from which the shared surfaces are lined with human ECs to mimic blood vessels.[22,24–26] Other studies have used channels that are cast in full collagen type I gel to mimic the lymphatic vessels or to study skin cell interaction with blood vessels.[27–29]

Despite development of these highly advanced systems, several challenges in blood vessel-on-a-chip design remain, such as optimization of a protocol that would allow addition of mural cells to the endothelial monolayer.[14–16,19,27,30,31] Vascular-supporting cells, particularly pericytes that are present in the native microvasculature, play a significant role in establishing vascular homeostasis and maintaining the barrier function.[32,33] Pericyte deficiency in specific murine knockdown lines results in significant loss of endothelial barrier function, causing vascular leakage, and reduced vascular growth.[34–36] Inclusion of perivascular cells into the vessel-on-a-chip system is therefore a crucial requirement to fully emulate the functional human microvasculature.

The use of micro-channels fully cast in PDMS with the (endothelial) cells directly cultured on a PDMS surface[12,13,37,38] also provides another challenge; PDMS has different properties than native ECM in context of stiffness and bio-stimulation of (endothelial) cells, and limits the natural interaction between mural cells and ECs.[39,40] However, PDMS does provide the right amount of mechanical stiffness to support physiologically relevant levels of flow in small caliber channels (<1000 μm) without compromising the channel geometry, which is often an encountered issue with perfusion of hydrogel-based channels. Most current models also do not use mechanically applied flow, but a passive low flow system based on volume differences in the in- and outlet reservoirs to circumvent these problems in hydrogel based channels.[41–43] The development of a novel vessel-on-a-chip system with controlled, unidirectional, continuous flow at levels that more closely mimic the physiological condition would greatly aid in the study of typical circulating immune cell behavior during interactions with the vasculature such as rolling, adhesion and extravasation.[5,6]

Here we present a new advanced *in vitro* microfluidics model that more closely mimics the *in vivo* vasculature by: (1) creating a mechanically controlled perfusion system with multiple tubular micro-channels that are completely enclosed in 3D ECM without direct contact of seeded cells with the PDMS casing or any other hard-material scaffolding. (2) Seeding these channels with human-derived GFP-labeled ECs and dsRED-labeled pericytes, and thereby recreating a blood vessel with a confluent endothelium and mural cell support providing optimized endothelial barrier function. (3) Controlling perfusion with circulating immune cells through these neovessels to provide a platform for interaction studies of circulating cells with the activated endothelium. This new system is designed to allow spatiotemporal visualization of the multiple steps in leukocyte adhesion *in vitro* using confocal microscopy with the possibility of live imaging. It can be used to enhance our understanding of the mechanisms of vascular inflammation processes in various diseases.

Materials and methods

Cell culture

Human umbilical vein endothelial cells (HUVECs; Lonza) were cultured in EGM-2 (EBM-2 supplemented with Single

Quots; Lonza). Human brain derived pericytes (ScienCell) were cultured in DMEM (Gibco) with additional 10% FBS (GE healthcare). All media was supplemented with 100 U ml^{-1} penicillin/streptomycin (Gibco). Cells were cultured on fresh gelatin (Sigma-Aldrich) coated dishes until passage 8 and harvested using trypsin (Gibco). Lentivirus green fluorescent protein- (GFP) transduced HUVECs and lentivirus discosoma sp. Red fluorescent protein- (dsRED) transduced pericytes (both under the human EF1a promoter) were used until passage 8. GFP-transduced HUVECs and dsRED-transduced pericytes show bright fluorescence in their cytoplasm. Dead cells will not express any fluorescent signal. THP-1 cells were kept in suspension culture using RPMI (Gibco) with the addition of 10% FBS (GE healthcare) and 1% penicillin/streptomycin (Gibco) until passage 23. All cells and experiments were incubated at 37 °C with 5% CO_2.

Microfluidic device manufacturing

A microfluidic device mold was designed in NX version 10.0 and milled with a Roland MDX-40a benchtop CNC Mill from polymethylmethacrylate (PMMA). Twenty seven G needles (BD Bioscience) were glued into 21G needles (BD Bioscience, New Jersey/United States) with metal–metal epoxy glue (Bison). PMMA mold and needles were cleaned and assembled to form the microfluidic mold. Sylgard 184 elastomer polydimethylsiloxane (PDMS; Dow Corning) was prepared in a 1 : 10 curing agent to base ratio, stirred and placed in a vacuum dissector until all air was removed. PDMS was poured into the PMMA-based microfluidic device mold and placed in a 65 °C oven for at least 2 hours. After peeling off the PDMS from the mold, a glass coverslip was assembled to the PDMS device. Both, the PDMS component and the glass coverslips (22 × 22 mm) (Paul Marienfield, GmbH & Co) were tape cleaned for dust and the bonding surface was treated with corona discharge (SpotTEC, Tantec) prior to assembly. Furthermore, the bonded microfluidic devices were put in 65 °C for 30 min with additional weights to reinforce covalent bonds. Freshly formed covalent bonds between glass and PDMS results in a leakage-free microfluidic device. The reservoir is 5 mm by 17 mm by 1.7 mm in a PDMS device of 21 mm by 41 mm. Needles for molding the ECM gel channels were located at a distance of 0.75 mm of the bottom.

Fibrinogen gel creation and channel molding

ESI† Fig. S1 illustrates the work flow overview. PDMS devices were sterilized with UV for 30 min. Five sterile 26G needles (450 μm in diameter, BD bioscience) were inserted in the ports of the PDMS and function as the molds for casting the channels. Fibrinogen (7.5 mg ml^{-1}; Millipore) was dissolved in EGM-2 (Lonza). Vacuum was applied to remove air bubbles in the ECM containing. Next, a pericyte pellet was resuspended in the fibrinogen solution to a concentration of 5×10^5 cells per ml which was injected into the reservoir of the sterile PDMS microfluidic device *via* a syringe and 30G needle (BD Bioscience). A 30G needle on the opposite site of the reservoir acts as outlet for air (ESI† Fig. S1). Devices with ECM gel and pericytes were placed in an incubator and turned over every 30 min for 2 hours, before leaving in the incubator overnight for further crosslinking. Needles were removed after 24 hours subsequently forming channels in the ECM gel (indicated in all further experiments as day 0). HUVECs were concentrated to a 12×10^6 cells per ml suspension in EGM-2 and seeded into the formed channels. The PDMS device was turned over every 30 min to evenly seed the top and bottom of the channels. After 2 hours, the microfluidic device was submerged in EGM-2 (static condition) for three days to ensure the HUVECs formed a monolayer in the channel. Based on the reservoir volume and channel volume (all 5 channels combined) and the previously described cell concentrations, the estimate ratio between pericyte and HUVECs is 1 : 4.2 (12 560 pericytes *vs.* 52 800 HUVECs) per microfluidic device. All experiments were conducted 3 days after seeding HUVECs in the channels after visual validation of successful endothelial monolayer formation.

Perfusion set up

The Ibidi perfusion sets (black; Ibidi) were fitted with an additional PE-50 (Becton Dickinson) with inner diameter of 0.5 mm in order to match the specifications of the inlets of the PDMS mold. All perfusion sets were sterilized with 70% ethanol and UV radiation for one hour. The connection of the perfusion set with the microfluidic device was made with the PE-50 tubing and needles. Sterile 26G needles were inserted before the perfusion in the PDMS. The points of the needles reach the start of the HUVECS channel in order to keep residual PDMS from closing the channel and disturbing the flow. The setup was placed in an incubator and flow speed was adjusted using the Ibidi pump software. Perfusion with THP-1 cells was performed with a combination of culturing media, in ratio 1 : 1 of EGM-2 and RPMI (further referred as perfusion medium). THP-1 cells (5×10^5 cells per ml in total) were stained with CellTracker Deep Red Dye (Thermo Fisher) according to manufacturer's manual and used for perfusion. Cells were kept in perfusion medium after staining. Tumor necrosis factor (TNFα 10 ng ml^{-1}; rhTNFα, R&D systems) or control (PBS) in perfusion medium was added to the THP-1 perfusion.

In-channel immunofluorescent staining

Immunofluorescent staining was performed at specific time points. The PDMS device was fixated by submersion in PFA 4%. 1% BSA (bovine serum albumin), primary antibody (anti-VE-cadherin (CD144) clone BV9, Millipore), secondary antibody (Alexa Fluor® 568, Invitrogen Life Technologies) and DAPI were applied with caution using a 30G needle. After each injection step, a wash step was performed 3 times by submerging the channels in PBS. VE-cadherin primary antibody targets extracellular parts of VE-cadherin and was

incubated overnight at 4 °C before incubation with the secondary antibody for 1 h at room temperature.

RNA isolation and qPCR

RNA from the cells in the microfluidic device was isolated in 2 ways, either as a pool of HUVECs and pericyte RNA (1), or per individual cell type (2). For condition 1: the PDMS casing was cut open to gain access to the reservoir. The full reservoir (ECM gel including pericytes and HUVECs) was lysed using RLY lysis buffer for RNA isolation. For condition 2: RLY lysis buffer was flushed into the channel using a syringe and needle in the inlet and outlet of the microfluidic device. Lysate from all channels was combined for RNA isolation to form the HUVECs specific fraction. The remaining gel with pericytes in the microfluidic device was lysed, creating a separate pericyte fraction. RNA was isolated using ISOLATE II RNA kit (Bioline) with DNAse and cDNA was made using SensiFAST cDNA synthesis kit (Bioline) according manufactures protocol. qPCR was performed using FastStart Universal SYBR Green Master (Roche) following the qPCR program: 8,5′ 95 °C, 38 cycles (15″ 95 °C; 45″ 60 °C) 1′ 95 °C, 1′ 65 °C, 62 cycles (10″ 65 °C + 0.5 °C). Gene expression levels were normalized to β-beta actin (ESI† Table S1).

Dextran diffusion assay

Dextran rhodamine B 70 kDa (10 nM in PBS; Sigma-Aldrich) was used to address endothelial barrier function. Dextran was initially applied to the cell seeded channels of the microfluidic device in the presence or absence of human recombinant thrombin (0.5 and 1 U ml^{-1}; thrombin, R&D systems).

Imaging

Imaging of the microfluidic device was performed with a Leica TCS SP8X confocal microscope. Due to the dimensional properties of the channels, images were made with 10× or 20× magnification for both z-stack mode (42 focus sections per z-stack, 12 μm step size) and tile scan mode (3 × 2 tile). Average confocal time for each channel was 45 min using these settings. Images shown are projections of these tile scan/z-stack images unless indicated otherwise. Image analysis was performed with Leica LASX software and ImageJ. Longitudinal cross sections, 3D reconstructions, and GIF movies of the channels in the microfluidic device were generated with Leica LASX software. Dextran diffusion assays and channel width measurements were performed with an inverted microscope (Olympus IX53). Immediately after dextran injection, the channels were imaged every 10 min. Image analysis and quantification was performed using ImageJ and Graphpad Prism software (version 7.02). Dextran permeability coefficient was calculated according to the method published by Price and Tien.[44]

Statistics

All data shown in bar graphs are presented as means ± SEM. Groups were compared by students *t*-test or one-way ANOVA followed by Tukey *post hoc* test when appropriate. $P < 0.05$ was accepted as statistically significant.

Results

Microfluidics device design, production, and use

The microfluidic device is composed of an open reservoir made of PDMS walls and a bottom that is sealed with a coverslip. This reservoir is filled with ECM gel (fibrinogen in the present study) and is connected to 5 inlets and 5 outlets in the PDMS walls that can be linked to tubing for monitored perfusion. These connectors narrow down to 450 μm diameter sections towards the reservoir. The schematic device design is shown in Fig. 1A and prototype replicated PDMS device is shown in Fig. 1B. A fibrinogen gel mixed with (dsRED-labeled) pericytes is injected through the PDMS into the reservoir to form the ECM gel. The reservoir offers the possibility to cast different types of ECM gels, with or without additional cells, to mimic the microenvironment. In total, five 26 gauge needles are inserted through the inlets and outlets to act as molds during the casting of the fibrinogen gel to create 450 μm diameter channels in the 3D ECM. After gel cross-linking, the needles are extracted, leaving behind the open channel structures (Fig. 1C). The five individual ECM channels are aligned with the PDMS inlets and outlets, creating a closed leakage-free system that allows flow perfusion of the ECM channels using tubing connected to the Ibidi pump system (Fig. 1D i and ii). The channels are seeded with GFP-labeled HUVECs to create the endothelial monolayer lining of the blood vessels. A schematic overview of the workflow, including a time line (ECM casting; day-1, EC seeding; day 0, maturation of the channel and start experiment; day 3), is shown in ESI† Fig. S1. Quantification of channel diameter shows a limited ~60 μm (~12%) increase in channel diameter immediately after needle removal (Fig. 1E). Other procedures, such as seeding of the channels with HUVECs, prolonged static culture and flow perfusion did not further influence the channel diameter. Using this setup, the device offers a biocompatible, homogenous, isotropic, and optically transparent setting that is suitable for direct observation of the ECM channels by (fluorescence) microscopy in real-time. The distance from the center of the ECM channel to the cover glass is 0.9 μm, which places the entire channel within the working distance of a high-resolution lens on standard confocal microscopes. This arrangement allows direct monitoring and recording of dynamic interactions of vascular and circulating cells in the 3D blood vessel structure.

Bio-engineering of a mechanical flow perfused blood vessel in the fibrinogen matrix environment of the microfluidic device

The human blood vessel is composed of a confluent monolayer of ECs supported by mural cells such as pericytes.

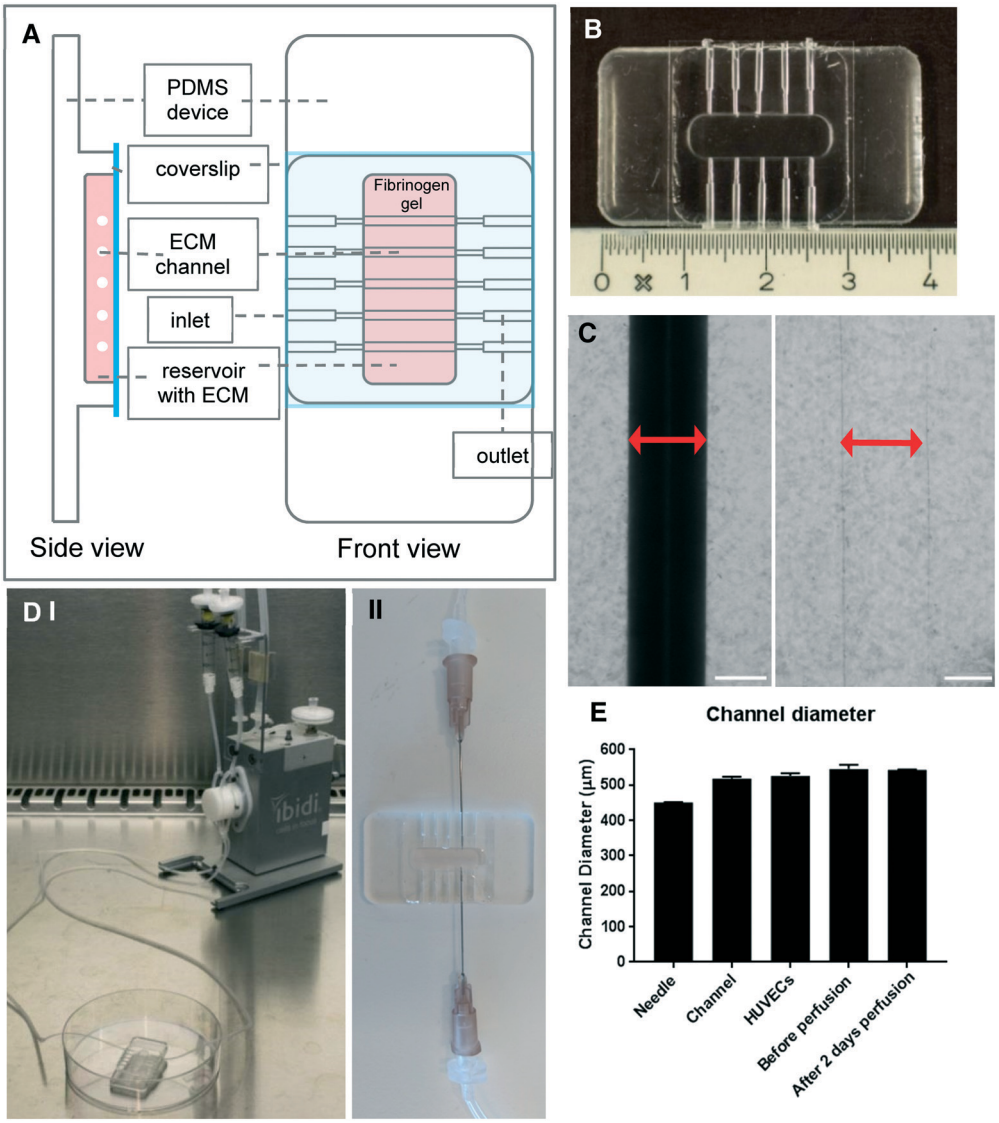

Fig. 1 Microfluidics device design, production, and use. (A) Overview of the design of the microfluidics device. (B) Prototype of the microfluidics device. (C) Micrographs show on the left hand side the needle embedded in the fibrinogen gel, and on the right hand side the ECM channel left behind in the crosslinked fibrinogen matrix after removal of the needle. Diameter of the channel is indicated by a red bar. (D; I and II) Setup of the microfluidics system connected to the Ibidi perfusion pump *via* needles and tubing. (E) Bar graph showing the ECM channel diameter in the presence of the needle, after removal of the needle (channel), after seeding with HUVECs in the channel (HUVECs), before perfusion (3 days after seeding) and after 2 days of perfusion (40 µl ml^{-1}). *N* = 3. Scale bar = 250 µm.

To evaluate ECs and pericytes behavior, we co-seeded the microfluidic system with both cell types. GFP-labeled HUVECs directly seeded into the ECM channels of the device developed confluent monolayers in 3 days time under static conditions (Fig. 2A, view from bottom side of vessel wall). Monitoring the same channels from day 1 to day 3 reveals a steady increase of ECs till full coverage at day 3. Meanwhile dsRED-labeled pericytes, homogeneously seeded in the fibrinogen matrix, were increasingly recruited to the neovessel over time (ESI† Fig. S2A). In contrast, in conditions in which only HUVECs-GFP were seeded in the channels without pericytes in the ECM, ECs coverage of the channels remained poor with the cells showing difficulties to maintain a confluent monolayer (ESI† Fig. S2B).

The neovessel structures created by co-culture of HUVECs and pericytes maintained an open lumen as shown in the longitudinal and composite views (Fig. 2B and C; ESI† Fig. S2C, ESI† Movie 1). At day 3, some dsRED-labeled pericytes made direct contact with the endothelial monolayer, as shown in the 3D composite (Fig. 2D) and high magnification (Fig. 2E i and ii) views. Experiments to evaluate the sprouting capacity of the established neovessel also showed pericyte coverage of the emerging endothelial sprouts (ESI† Fig. S2D, Movie S2).

Flow perfusion was introduced in the microfluidics device by connecting the inlets and outlets with tubing in a closed system connected to an Ibidi pump. The ECM channels were first perfused with medium at 20 µl per minute and

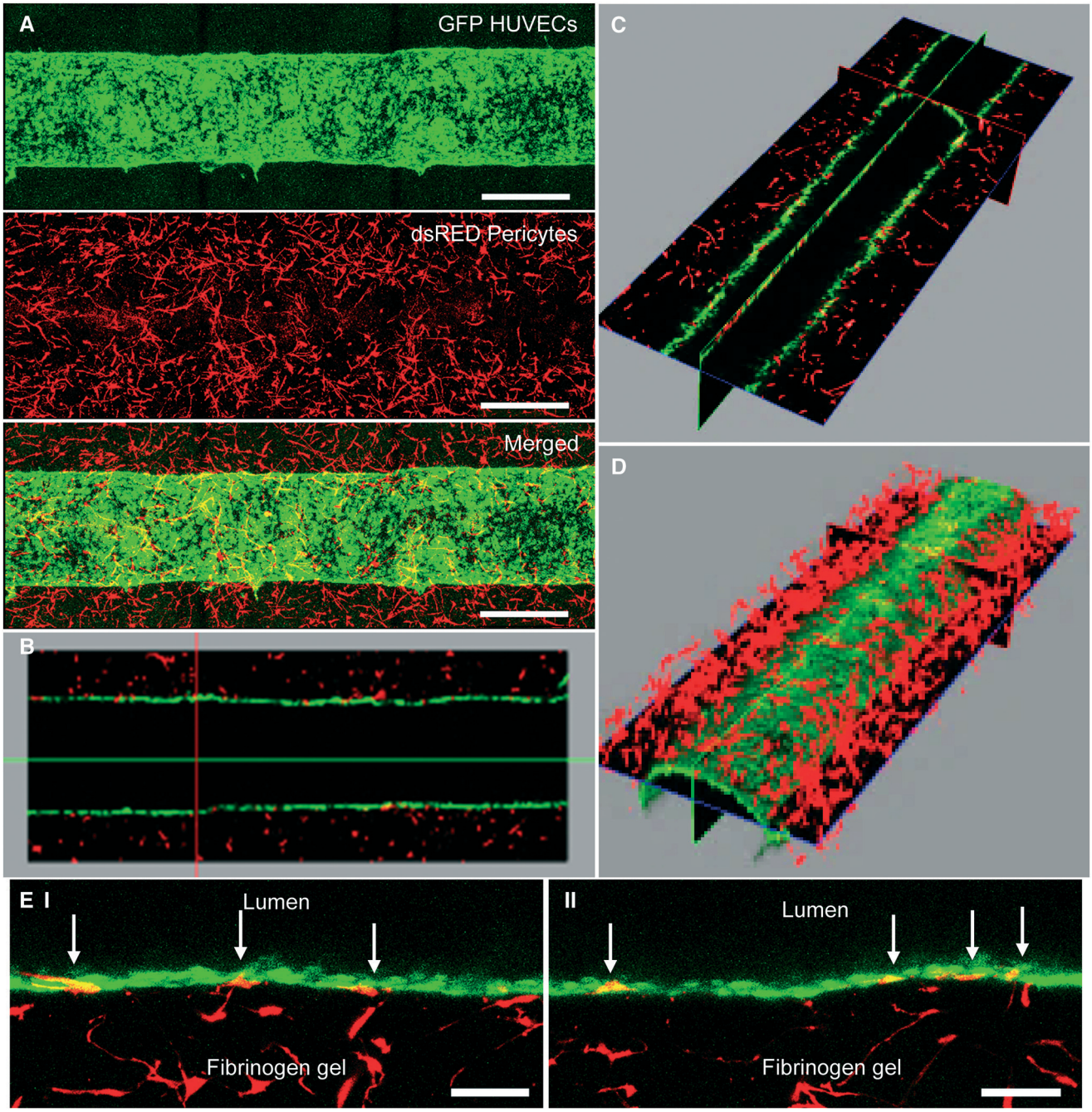

Fig. 2 A complex neovessel with open lumen is formed in the ECM channels after 3 days of static co-culture after cell seeding. (A) Confocal micrograph of the endothelial monolayer formed by GFP-labeled HUVECs (green) with perivascular coverage by dsRED-labeled pericytes (red) of the artificial neovessel. Scale bar = 500 μm. (B) Longitudinal cross section of the vessel. (C) Composite display of longitudinal cross section micrographs. (D) 3D reconstruction of half a wall of the neovessel. (E; I and II) High magnification views of the vessel wall. Pericytes are localized in direct contact with ECs, indicated by white arrows. Scale bar = 250 μm.

incubated at 5% CO_2 at 37 °C to allow the ECs monolayer to adjust from a static condition to flow. After 24 h, the flow rate was increased to 40 μl min^{-1}, which yields an estimated shear rate of 38.3 s^{-1} or a wall shear stress of 0.286 dyne per cm^2. This is close to, or within the range of, the levels previously used in microfluidic studies that focus on leukocyte–endothelium interaction under controlled flow.[45–47] After 2 days of controlled continuous perfusion at 40 μl min^{-1}, the endothelial coverage of the seeded ECM channels remained fully confluent and perivascular pericyte coverage of the neovessel remained intact (Fig. 3A and B).

To assess in more detail if prolonged culture and/or flow improves the number of recruited pericytes to the direct neovessel ECM surroundings and subsequent promote neovessel coverage, quantification of the dsRED signal was conducted in co-cultures at 4- and 5-days post seeding. A

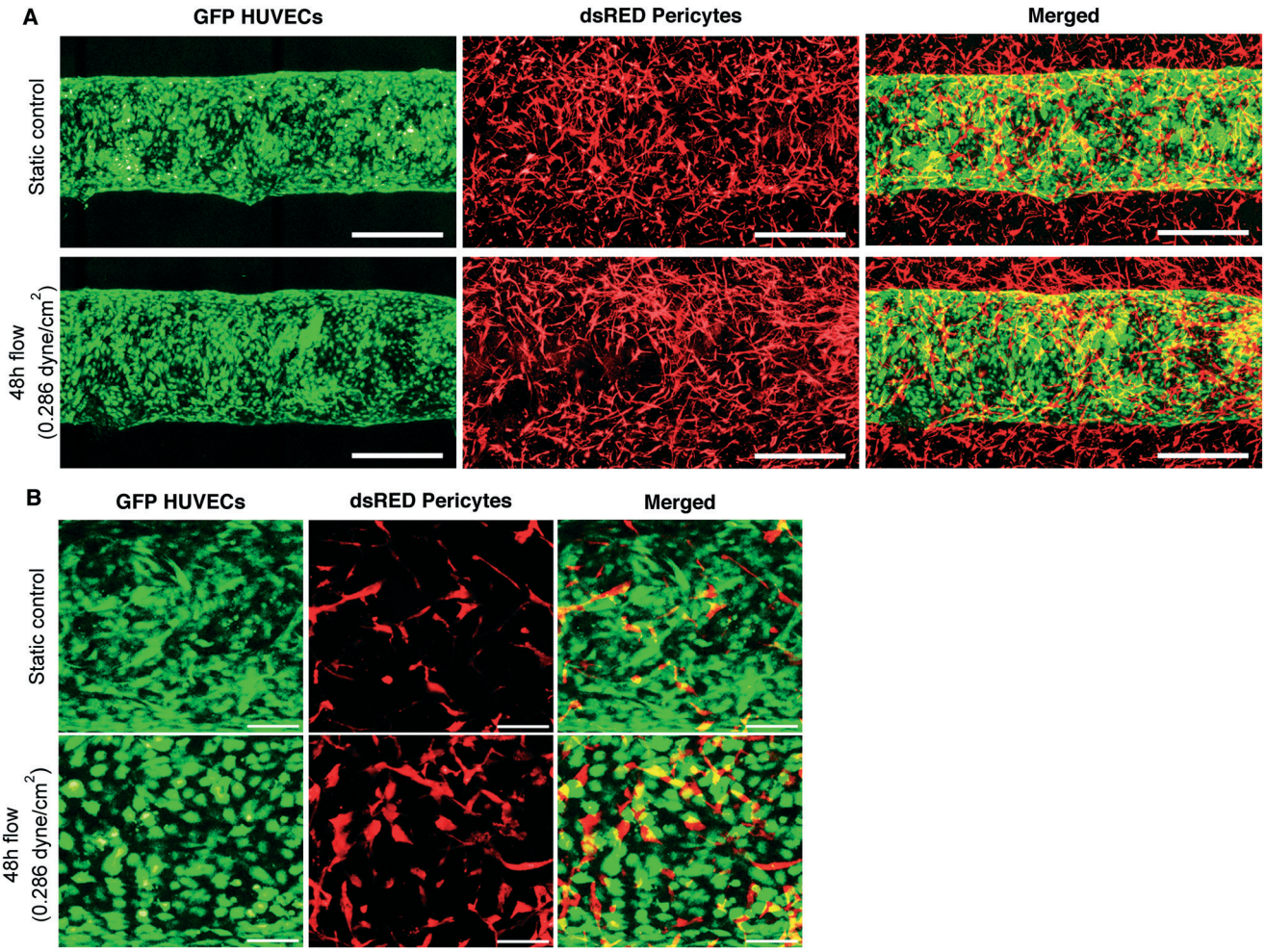

Fig. 3 Flow perfusion of the neovessels in the microfluidics device. (A) Micrographs show the monolayer of GFP-labeled HUVECs and perivascular coverage of dsRED-labeled pericytes of the neovessels after 5 days of static culture (upper row) and after 3 days of static culture + 2 days of flow perfusion (0.286 dyne per cm^2, 40 μl ml^{-1}, lower row). Scale bar = 500 μm. (B) High magnification images of static culture (upper row) and perfused (lower row) neovessels. Scale bar = 100 μm.

steady increase of pericyte area per standardized image view was observed when comparing day 4 and 5 with day 3 post seeding under static conditions (Fig. 4A and B). No additional effect on pericyte area in the neovessel surrounding ECM was observed when flow was applied at day 4 (Fig. 4B). The increased coverage over time was not attributed to adaptations in cell morphology and subsequent increase per individual pericyte cell surface area, but is associated with an increase in total pericyte number (ESI† Fig. S2E). This increase in the amount of pericytes stabilized after 7 days of static co-culture (data not shown).

The time-dependent increase in local accumulation of pericytes was more pronounced closer to the endothelial wall (Fig. 4C). To analyse pericyte distribution, different segments were defined, ranging from 0–200, 200–400, 400–600 μm from the vessel wall into the ECM gel, with 0 assigned to the location nearest to the vessel wall. Quantification of pericyte + areas in each segment showed that there are more pericytes present within the segments closest to the neovessel after 5 days of static culture (Fig. 4D and E). This typical distribution pattern persists after prolonged incubation (*e.g.* day 9) of the microfluidic device (data not shown).

Prolonged co-culture of pericytes with ECs in the microfluidic system did not diminish the pericyte phenotype, as shown by assessment of expression levels of typical pericyte markers PDGFRB and NG2 over a period of 7 days, in whole neovessels and ECM lysates. At 7 days post seeding, a significant increase in mRNA levels of both pericytes markers was observed compared to earlier time points (Fig. 4F). Similarly, prolonged co-culture in the device did not diminish the EC phenotype, as shown by stable mRNA levels of typical endothelial markers VEGFR2 and PECAM (Fig. 5A). Likewise mRNA levels of adherens junction VE-cadherin, tight junction ZO-1 and gap junction connexin 43 (CX43) remained constant during the 7 days of co-culture (Fig. 5B).

To specifically evaluate the expression of cell junction markers by ECs that comprise the monolayer in the neovessels, separate lysates for RNA isolation of ECs in the channels and pericytes in the gel were harvested. ECs and pericytes enrichment of the harvested fractions was validated

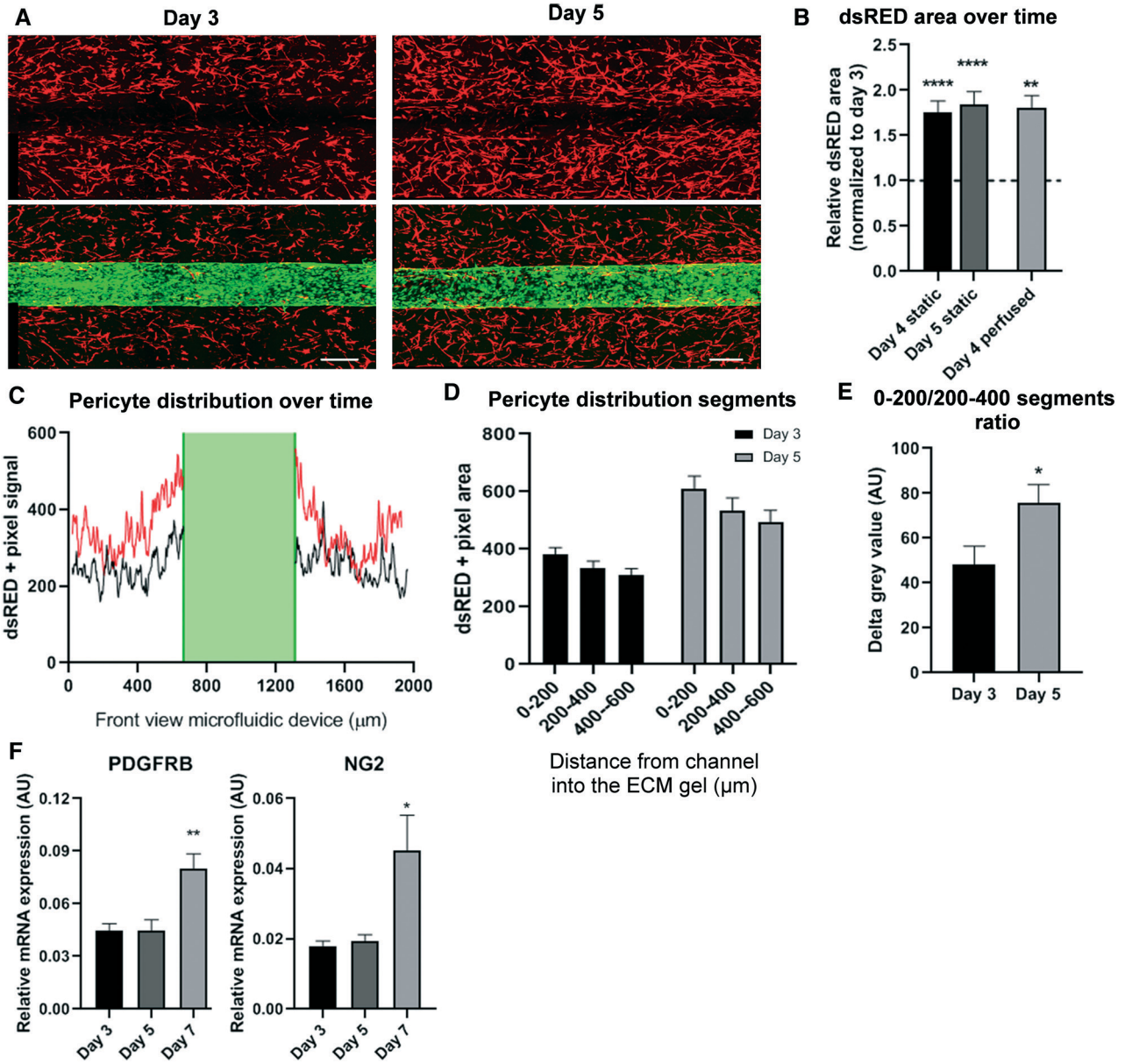

Fig. 4 Pericyte characteristics over time. (A) Representative projection of dsRED pericytes (upper picture) and merged with GFP endothelial cells (green; lower picture) signals at day 3 and day 5 of culture under static conditions. Scale bar = 250 μm. (B) Increase of pericyte dsRED area over time and after flow: total dsRED area per image view are displayed for day 4 (n = 6) and day 5 (n = 14) under static conditions and 1 day after perfusion (day 4; n = 5). Day 4 and 5 (both static) and day 4 perfusion (1 day of perfusion) are normalized to their starting point, day 3 (dotted line). $^{**}P < 0.01$, $^{****}P < 0.0001$. (C) Representative view of changes in pericyte distribution over time. Average dsRED signal (grey value) of day 3 (black line) and day 5 (red line) quantified in a cross section perpendicular to the neovessel. The green area represents the neovessel area. Beside the higher signal of pericytes at day 5 (due to increase in numbers), the distribution of the pericytes is more shifted to the vicinity of the neovessel compared to day 3. (D) Changes in pericyte distribution over time in different locations in close and distant proximity of the neovessel. To analyse pericyte distribution, different segments were defined ranging from 0–200, 200–400, 400–600 from the neovessel wall into the ECM gel, with 0 nearest to the vessel wall. The graph shows the average pericyte area (grey value dsRED) of the different segments at day 3 and day 5. Pericyte area at day 5 is increased compared to day 3, due to increase in pericyte numbers. (E) Significant increase in pericyte recruitment towards the vessel wall over time. To analyse the changes in pericyte recruitment towards the 0 baseline location (vessel wall), changes in pericyte area in segment 0–200 and 200–400 were assessed as calculated by the delta of area values in segments 0–200 *vs.* 200–400 at day 3 (black bar graph) compared to day 5 (grey bar graph). N = 6, $^{*}P < 0.05$. (F) mRNA levels for well-known pericyte markers PDGFRB and NG2 over time. Both genes were significantly upregulated at day 7 compared to earlier time points. N = 5, $^{*}P < 0.05$, $^{**}P < 0.01$.

by qPCR evaluation of ECs and pericytes markers (ESI† Fig. S3A). The ECs enriched fraction showed a trend (P = 0.099) of higher VE-cadherin expression compared to 2D mono cultured ECs and comparable expression levels to ECs co-cultured with pericytes in a trans-well setup (ESI† Fig. S3B). Fluorescent immunostaining of VE-cadherin of the

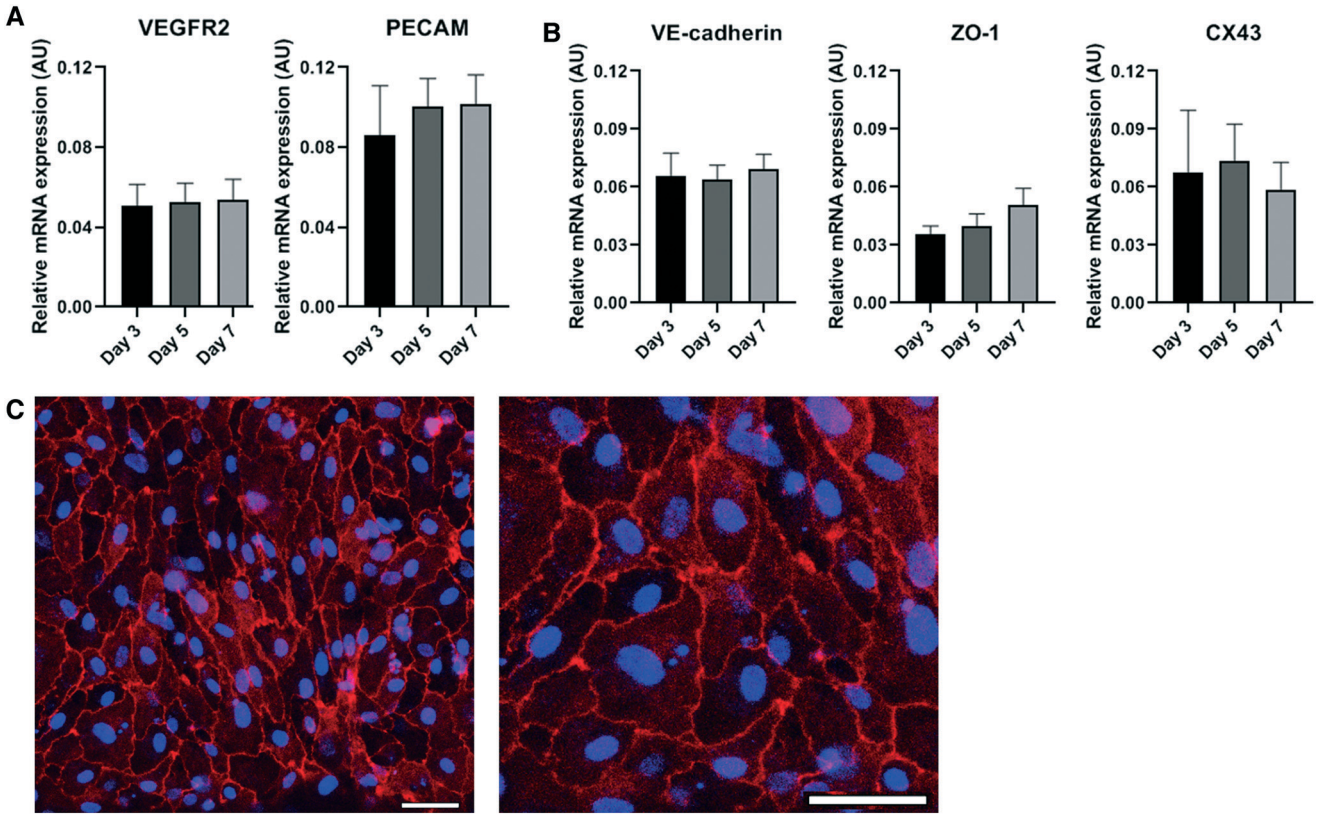

Fig. 5 Endothelial characteristics over time. (A) Stable mRNA levels of well-known endothelial cells markers VEGFR2 and PECAM over time. (B) Stable mRNA levels of junction markers VE-cadherin, ZO-1 and CX43 over time. All graphs are $N = 5$, except ZO-1 ($N = 4$). (C) VE-cadherin staining of the endothelial monolayer of the neovessel. VE-cadherin junctions (red) are clearly visible between the endothelial cells. DAPI signal (blue) stains cell nuclei. High magnification image (right) shows the VE-cadherin junctions between endothelial cells and DAPI$^+$ nuclei. Scale bar = 50 μm.

neovessels in static co-culture conditions showed well-established adherens junctions in the endothelial monolayer (Fig. 5C), indicating successful establishment of an intact endothelial barrier.

Assessment of endothelial barrier function

An important function of the endothelium *in vivo* is to form an active, regulatory barrier between the vessel lumen and the surrounding tissue for relatively large sized plasma proteins and circulating cells. Therefore, we assessed the endothelial barrier function of the established ECs monolayer in the ECM channels by monitoring the *trans*-endothelial diffusion of rhodamine labeled 70 kDa dextran during static culture conditions at 3 days post seeding in the microfluidic device. ECM channels without coverage of HUVECs and pericytes showed dextran leakage into the ECM environment at 1 min after onset of dextran injection. Fluorescent dextran signal was increased after 30 min. Similarly, coverage of ECM channels with HUVECs only produced considerable dextran leakage at 1 and 30 min post perfusion time points. In contrast, coverage of ECM channels with HUVECs and pericytes clearly reduced dextran leakage at 1 and 30 min after onset of dextran perfusion compared to the other two conditions (Fig. 6A). The fluorescent area of the dextran rhodamine signal that has penetrated into the surrounding ECM was quantified per cross-sectional location and displayed in bell-curve graphs for 1 and 30 min measurements. The slopes for the 1 and 30 min bell-curves of the 'HUVECs + pericytes' condition were considerably steeper than the slopes of the 'no cells' and 'HUVECs single' conditions, indicating that dextran rhodamine signal was more maintained within the ECM channel when the device was seeded with both HUVECs and pericytes (Fig. 6B). Quantification of the area under the bell-curve (AUC), showed a significant increase in dextran area inside the channel for 'HUVECs + pericytes' *versus* 'HUVECs single' or 'no cells' conditions at 30 min after onset of dextran perfusion (Fig. 6C). In line with these findings, the AUC shows a significant increase in dextran area outside of the channel for 'no cells' and 'HUVECs single' *versus* 'HUVECs + pericytes' conditions at 30 min after onset of dextran perfusion (Fig. 6D). The calculated permeability coefficients derived from these data similarly shows a reduction in dextran leakage between 'HUVECs + pericytes' compared to 'HUVECs single' (2.62×10^{-7} cm s^{-1} ± 2.45×10^{-7} cm s^{-1} *versus* 3.12×10^{-6} cm s^{-1} ± 4.26×10^{-7} cm s^{-1}; $P = 0.002$) and 'HUVECs + pericytes' *versus* 'no cells' (2.62×10^{-7} cm s^{-1} ± 2.45×10^{-7} cm s^{-1} *versus* 4.21×10^{-6} cm s^{-1} ± 4.7×10^{-8} cm s^{-1}; $P \leq 0.001$) conditions.

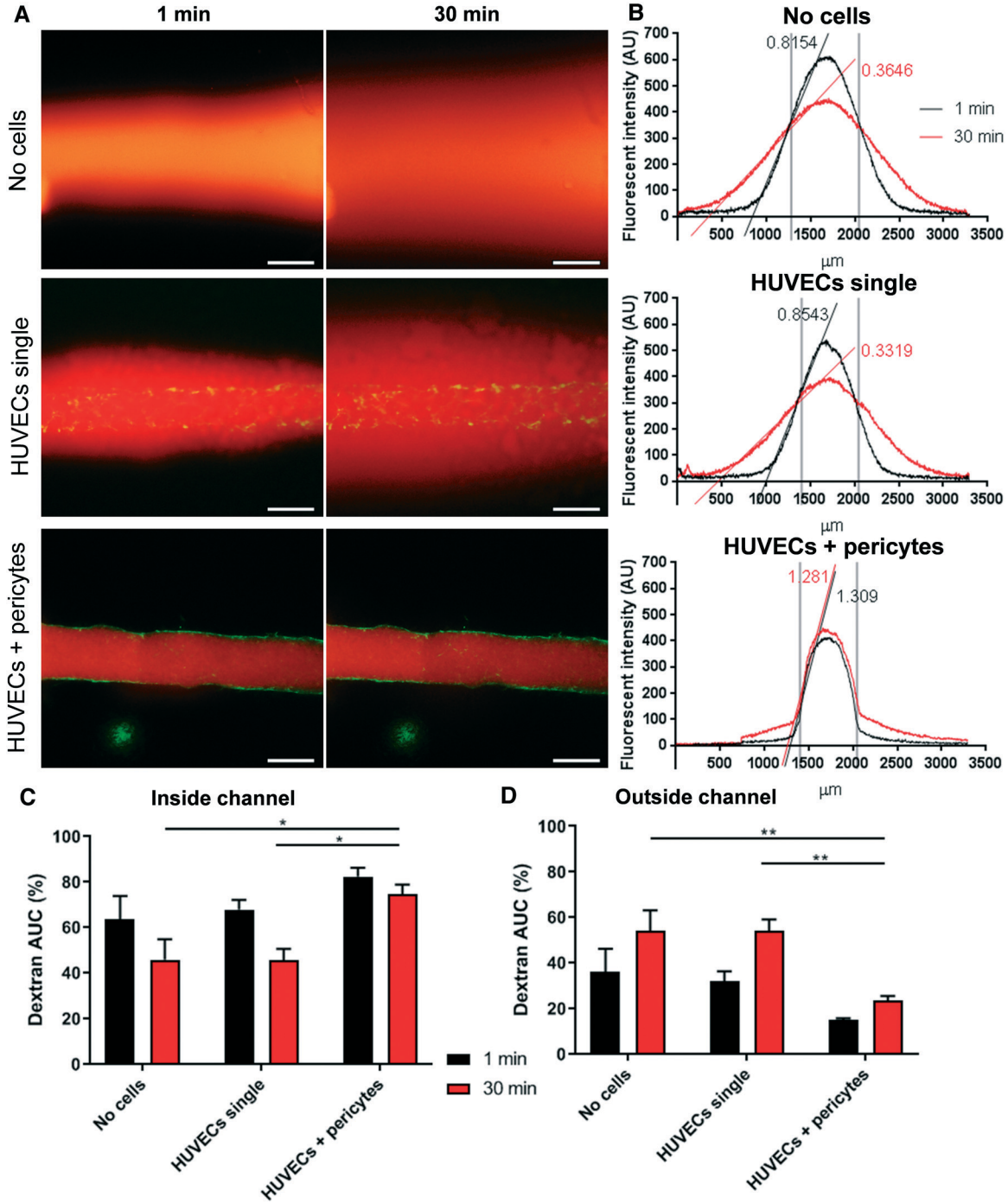

Fig. 6 Assessment of the endothelial barrier function of neovessels in the microfluidics device. (A) Micrographs show 70 kDa dextran rhodamine diffusion out of the vessel lumens at 1 minute and 30 minutes post dextran infusion into ECM in channels without cells (upper row), ECM channels seeded with single GFP-labeled HUVECs (mid row), and neovessels composed of GFP-labeled HUVECs and pericytes seeded in the ECM channels (lower row). Scale bar = 500 μm. (B) Cross-diameter bell-curve distribution of the fluorescent intensity of dextran rhodamine over the ECM compartment and channels for the different groups (without cells, with only GFP-labeled HUVECs, and with GFP-labeled HUVECs + pericytes), at 1 and 30 minutes post dextran rhodamine infusion. Slopes of the shoulders of the bell-curves are indicated in the graph. Quantified fluorescent intensity is shown on the *Y*-axes. Cross section location is shown on *X*-axes. The channel area is indicated by the grey lines in the graphs. (C) Bar graphs show the quantified data of dextran rhodamine + area under the curve (AUC) inside the ECM channel of the different groups (without cells, with only GFP-labeled HUVECs, and with GFP-labeled HUVECs + pericytes), at 1 and 30 minutes post dextran rhodamine infusion, in percentage of total curve area. $N = 4$, $^{*}P < 0.05$. (D) Bar graphs show the quantified data of dextran rhodamine + AUC outside of the ECM channels of the different groups (without cells, with only GFP-labeled HUVECs, and with GFP-labeled HUVECs + pericytes), at 1 and 30 minutes post dextran rhodamine infusion, in percentage of total curve area. $N = 4$ (1 channel from 4 different microfluidic devices), $^{**}P < 0.001$.

In circulating cells–vasculature interaction studies, endothelial activation compounds such as thrombin and TNFα are often used to induce a pro-inflammatory state in the endothelium. Consequently, thrombin was added to the dextran rhodamine solution to assess inflammation associated changes in endothelial barrier function.

The fluorescent area of the dextran rhodamine signal that has penetrated into the surrounding ECM was again quantified per cross-sectional location and displayed in bell-curve graphs for different doses of thrombin at different time points. Bell-curves of 0.5 U and 1 U thrombin addition to dextran at 1 minute, 30 min and 60 min after onset of dextran injection show a different distribution compared to control conditions (Fig. 7A). Quantification of the AUC shows a significant increase in dextran area outside the channel in the ECM in thrombin *versus* control conditions at the 30 and 60 min time points (Fig. 7B). However, the calculated permeability coefficient did not show a significant difference.

In addition, thrombin treated endothelial channels stained for VE-cadherin showed small disruptions of the adherens junction *versus* non-treated controls (Fig. 7C). These data show that the newly developed platform can be used to monitor and quantify vascular leakage over time and detect inflammatory cytokine induced alterations in endothelial barrier function.

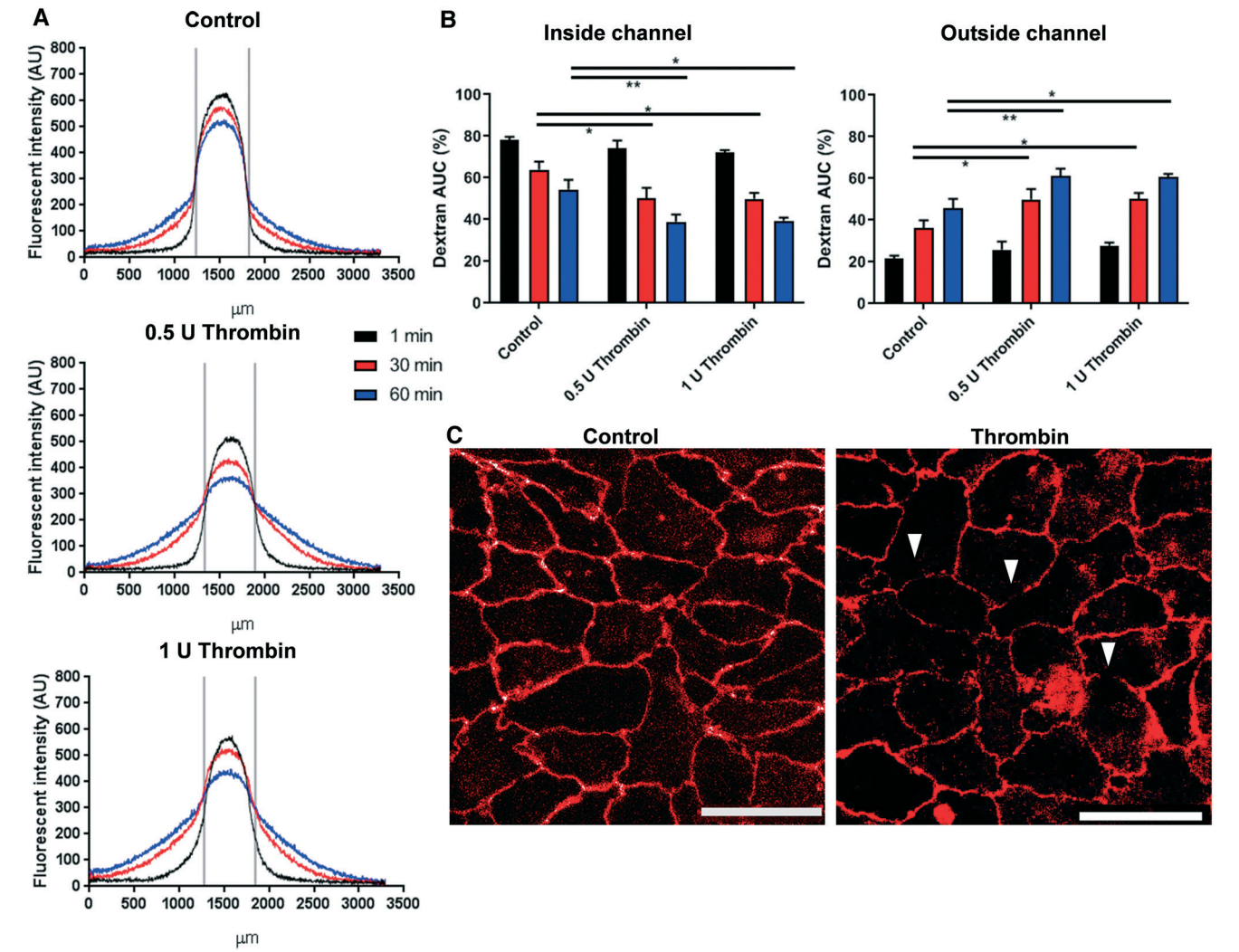

Fig. 7 Endothelial barrier function in the microfluidics device is responsive to thrombin stimulation. (A) Cross-diameter bell-curve distribution of the fluorescent intensity of dextran rhodamine over the ECM compartment and neovessels for the different groups (control, 0.5 U and 1 U thrombin), at 1, 30 and 60 minutes post dextran rhodamine infusion. Quantified fluorescent intensity is shown on the *Y*-axes. Cross section location is shown on *X*-axes. ECM channel area is indicated with grey lines in the graph. (B) Bar graphs show the quantified data of dextran rhodamine + area under the curve (AUC) inside (top graph) or outside vessel (lower graph) areas of the different groups (control, 0.5 U and 1 U thrombin), at 1, 30 and 60 minutes post dextran rhodamine infusion. $N = 4$ (1 channel from 4 different microfluidic devices), $^{*}P < 0.05$, $^{**}P < 0.001$. (C) VE-cadherin staining of the endothelial monolayer of the neovessels with and without thrombin stimulation. The control condition shows the clear line patterns of the VE-cadherin junctions between the endothelial cells (left). Thrombin stimulation results in small interruptions between the VE-cadherin junctions (white arrowheads). Scale bar = 50 μm.

Assessment of monocyte–endothelial interaction

One important aspect for a vessel-on-a-chip system to replicate for disease studies is the interaction between ECs and circulating (immune) cells. We assessed the interaction of circulating monocytes (THP-1) and the vascular wall in the presence and absence of pro-inflammatory cytokine TNFα. Flow perfusion was introduced as described above, but now with the addition of THP-1 cells in the perfusion medium. The perfusion medium was a mix of EGM-2 and RPMI medium to meet both ECs and THP-1 cells requirements. THP-1 cells were visualized with CellTracker deep red in combination with GFP-labeled HUVECs and dsRED-labeled pericytes. Circulatory cells remained in suspension in the Ibidi reservoirs and did not clog or stick to the Ibidi tubing. Endothelial channels were perfused with THP-1 cells for 24 h

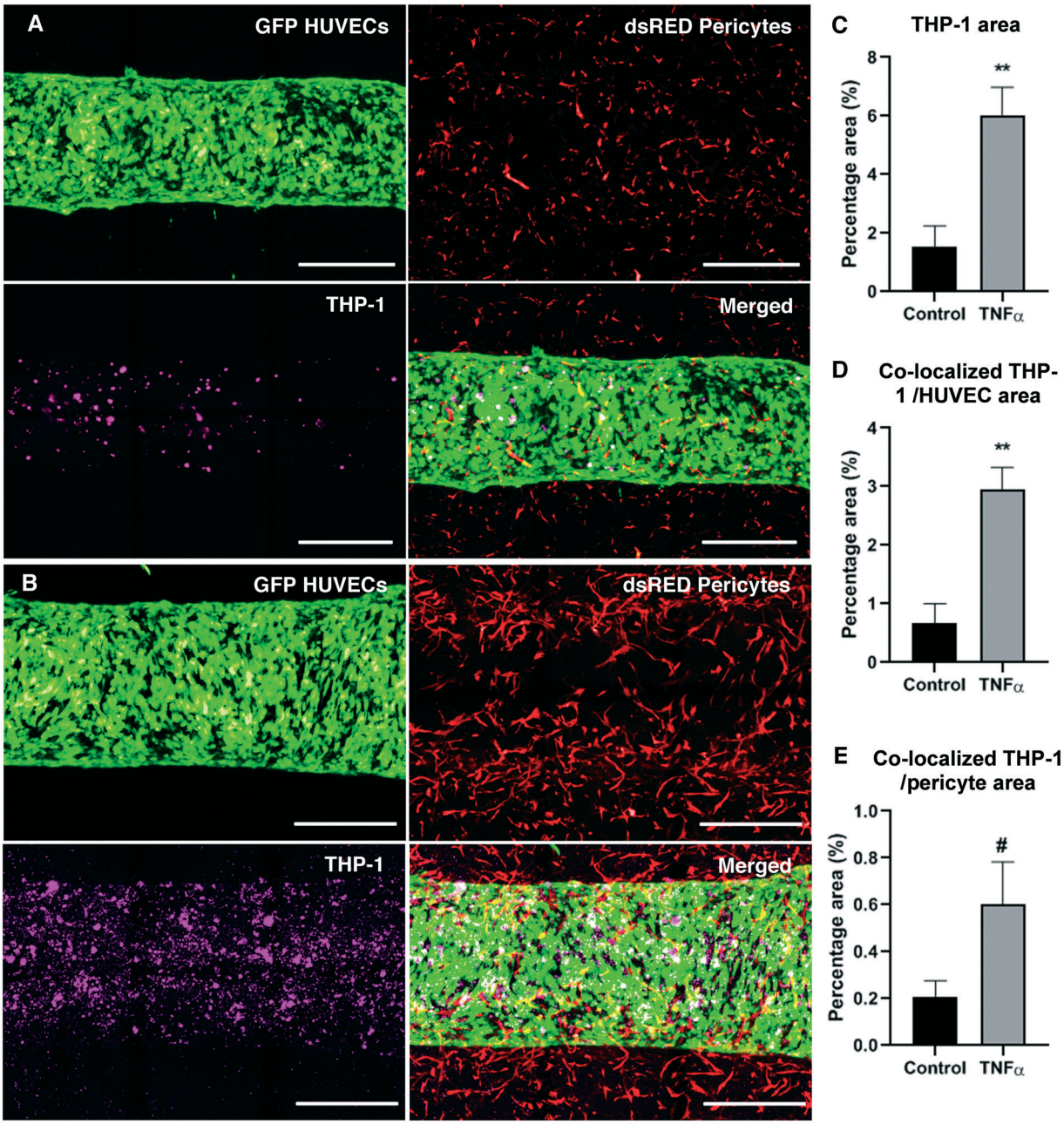

Fig. 8 Monocyte–EC interaction in response to pro-inflammatory cytokine TNFα after 24 hours perfusion. (A) Vessel wall shown after perfusion with medium with THP-1 cells (magenta) for 24 hours, shown are attached THP-1 cells. HUVECs are shown in green, pericytes in red. (B) Vessel wall after perfusion with THP-1 (magenta) for 24 hours in presence of TNFα. Scale bar = 500 μm. (C) THP-1 positive area shown in percentage of the total image area (displayed on *Y*-axes) is significantly increased in response to TNFα stimulation. (D) THP-1 positive area co-localizing with ECs is significantly increased in TNFα conditions. (E) THP-1 positive area co-localizing with pericytes shows a trend (#P = 0.0701) of increase when TNFα present. N = 6 (1 channel from 6 different microfluidic devices), **$P < 0.001$.

at 40 μl min^{-1}. Confocal microscopy showed live perfusion of THP-1 cells through the endothelial channel (ESI† Fig. S4A and B; Movie S3). A limited number of THP-1 cells attached to the endothelial wall under earlier described flow conditions (Fig. 8A). Addition of TNFα in the perfusion medium significantly increase attachment of THP-1 cells in these neovessels (Fig. 8B and C). Quantification of z-stack images showed increased co-localization of THP-1 cells and ECs with TNFα stimulation (Fig. 8D). TNFα did not influence THP-1 proliferation (data not shown). In addition, a trend (P = 0.07) is observed demonstrating an increase in percentage THP-1 area co-localized with pericyte area in TNFα conditions (Fig. 8E). TNFα did not influence total HUVECs or pericyte area, nor did it affect co-localization of HUVECs with pericytes (ESI† Fig. S4C and E). Binding of THP-1 cells to these neovessels in pro-inflammatory conditions illustrates that this *in vitro* microfluidic model emulates *in vivo* properties of the vasculature during inflammation.

Discussion

In this study, we designed, manufactured, and validated a novel microfluidic vessel-on-a-chip system that replicates complex, and most importantly, functional neovessel structures in a full 3D ECM environment. The most important findings of the present study are: 1) the ECM channels provide an excellent base to seed ECs to form tissue-engineered neovessels with relevant morphology and an open lumen supported by perivascular pericytes in a full 3D ECM microenvironment. 2) The endothelial monolayer inside the channels is maintained when exposed to controlled, unidirectional, continuous flow when perfused for up to 48 hours. 3) The created device provides an easily accessible platform for live confocal imaging of interaction between vascular cells, and (4) both pericytes and ECs contribute to a viable and functional neovessel. 5) The presence of pericytes in the microfluidic system is essential to maintain the endothelial barrier function of the tissue-engineered vessel, as monitored and quantified by using fluorescent labeled dextran perfusion. 6) Endothelial barrier function in the device is responsive to biological stimuli such as thrombin, making it a suitable platform for testing endothelial barrier function to different biological factors and pharmaceutical compounds. Furthermore, 7) circulating monocytes interact with the endothelial wall in response to the pro-inflammatory cytokine TNFα, demonstrating that the system is suitable for testing circulating leukocytes attachment to the endothelium during inflammation.

The low-cost and high throughput capacity of microfluidic technology could bridge the gap between *in vitro* and *in vivo* methods. We designed a microfluidic device that can easily be manufactured using standard PDMS casting techniques and can be used for live confocal imaging. The PDMS devices are highly reproducible due to the casting method and easy to handle during culturing and setup. This device enables the co-cultivation of multiple vascular cell types in a 3D fashion with ECM interactions, thereby mimicking the *in vivo* situation. Our current microfluidic platform supports two important readout parameters for the assessment of vascular function:

(1) Endothelial barrier function: our tissue-engineered vessel supported by pericytes establishes a functional monolayer which can be quantified using fluorescent labelled dextran diffusion. This method is often used in microfluidic systems to quantify vascular barrier function.[48,49] The calculated permeability coefficients of 2.62×10^{-7} cm s^{-1} and 3.12×10^{-6} cm s^{-1} for pericytes + ECs and only ECs conditions in our microfluidic system fall within the broad range reported by previous studies.[49–51] This level of permeability is higher than the levels observed *in vivo* models, yet lower compared to other *in vitro* models as indicated by Lee and colleagues.[51] In line with our data, Kim *et al.* observed a reduction in permeability when ECs were co-cultured with pericytes in their vessel-on-a-chip system.[52] Similarly Campisi *et al.* observed a reduction in permeability when pericytes were added to an iPSC derived endothelial culture in their blood brain barrier system,[21] with permeability further reduced when the authors used a combination of pericytes, iPSC ECs, and astrocytes.[21] Alimperti *et al.* also demonstrated the supportive role of bone marrow stromal cells in endothelial barrier function when these cells were co-cultured at different ratios with ECs, illustrating that pericytes are not the only dedicated cell types for vasculature support.[53]

Furthermore, our microfluidic model also responds to thrombin-induced ECs barrier changes: Thrombin stimulation disrupts VE-cadherin binding between ECs, thus decreasing the number of intact adherens junctions and impairing vascular barrier function.[54–56] Our data demonstrates that quantification of alterations in endothelial barrier function in response to thrombin is possible within a short time frame (1 hour) by assessment of dextran diffusion and VE-cadherin disturbance, which is line with a limited number of microfluidics systems that in their design offer a similar possibility to test endothelial barrier changes to thrombin.[53,57]

(2) Interaction with circulating immune cells under flow: circulating monocytes that show limited interaction with blood vessels during healthy conditions engage profoundly with the endothelium during inflammation, with leukocyte-rolling, -adhesion and -diapedesis mounting to an efficient first immune response at the inflammation site in response to multiple pro-inflammatory cytokines such as TNFα.[58–65] Our novel vessel-on-a-chip system allows pump-controlled, continuous, unidirectional perfusion of the tissue-engineered vessel with circulating cells, such as THP-1 cells, thus permitting live assessment of interaction of these cells with the endothelium in response to *e.g.* TNFα stimulation. Increased attachment of THP-1 cells to the vessel wall was observed in presence of TNFα after 24 hours, making the model suitable for studying immunological responses of the inflamed vasculature. TNFα levels vary greatly in different

inflammatory diseases. For example, rheumatoid arthritis patients show a modest rise to 17.9 pg ml^{-1} compared to patients with severe bone fractures (0.1 ng ml^{-1}).[66,67] Other groups found different TNFα levels in pre-eclamptic women (210 pg ml^{-1} *vs.* 1.93 pg ml^{-1}), clearly demonstrating the marked variation of TNFα levels reported in serum, even within the same disease, which could be due to differences in detection method or cohort group.[68] The concentration of TNFα used *in vitro* is usually much higher (range in ng ml^{-1}) compared to the serum TNFα levels measured *in vivo* during inflammation-related diseases, with the latter normally measured in the pg ml^{-1} range. The TNFα concentration that was used in the present study is well in line with other *in vitro* assays which assess monocyte adhesion and interaction with the ECs under flow in more traditional fluid-chamber settings.[11,65,69]

In the present study, a trend ($p = 0.07$) towards increased pericyte/THP-1 co-localization was observed when THP-1 were flowed in the presence of TNFα compared to control. Recent studies identified pericytes as important regulators in leukocytes extravasation.[70,71] $NG2^+$ subsets of pericytes constitutively express ICAM-1 on their membrane, whereas $NG2^-$ pericytes express ICAM-1 after TNFα stimulation.[71] Proebstl *et al.* showed that the occurrence of enlarged gaps between adjacent pericytes in response to inflammatory cytokines facilitates transmigration of leukocytes by binding to ICAM-1 expressing pericytes.[71] Ayres-Sander *et al.* confirmed the beneficial role of pericytes in trans-endothelial migration of neutrophils.[72]

Current model *vs.* existing state-of-the-art microfluidic models

The scientific community increasingly demands more complex 3D models that provide a more complete recapitulation of different vascular biological aspects. Currently, most research groups create their own microfluidic models using novel bio-fabrication methods with each model tailored to their specific research questions and needs.

When comparing our model to current state-of-the-art vessel-on-a-chip systems, our model provides some answers to previously encountered challenges in platform design, particularly in terms of vascular biology and constant flow regulation and perfusion. The advanced system presented by Takahashi *et al.* demonstrated a tubular channel seeded with HUVECs in a full collagen type I hydrogel environment in the absence of flow and mural cell incorporation.[14] The paper by Tan *et al.* presented a tubular channel seeded with human ECs in a full ECM environment with inclusion of vascular smooth muscle cells.[73] The use of other bio-fabrication techniques such as those developed by Jia *et al.* allows coaxial 3D printing to create a hollow tube composed of a bio-ink gel consisting of mainly gelatin-methacryloyl (GelMA) and 4-arm poly(ethylene glycol)-tetra-acrylate (PEGTA) in which a mixture of human mesenchymal cells and HUVECs are fully encapsulated in the tube wall.[74] These types of approaches successfully create a tubular structure with both ECs and mural cells. However, the organization of the cells remains an issue as high density GelMA is known to limit cell migration[75] and the formation of the distinct layers requires the ability of the cells suspended in the GelMA mix to self-organize into these layers. Similarly, Kolesky *et al.* also created a channel system in a full GelMA environment seeded with a monolayer of endothelial cells that could support endothelial barrier function.[31] However, although they combined this vascular network with other tissue cell types, mural cells were not incorporated and the system was not tested with pump-controlled, continuous flow.

In summary, the most recent studies reporting on vascular regeneration and vascular tissue on a chip all focus on improving different aspects ranging from how to increase complexity and biological function to assessment of different bio-fabrication methods for vascular structures. The majority of the published vascular microfluidic models share common features concerning bio-fabrication method, flow, 3D environment, ECM and types of cells used in culture. Most studies focus on a specific research question using a dedicated microfluidic model with predefined characteristics to test their hypothesis and thus, all have their own merits and limitations. For our vessel-on-a-chip system, we focus mainly on recreating a system with a biological environment that not only sustains vascular cells, but also supports a vascular response that mimics the natural conditions, including the capacity of the cytokine-activated endothelium to interact with circulating immune cells. Our system thereby offers a valuable complementary model to existing platforms, which are more orientated towards assessing *e.g.* sprouting capacity and interaction with tissue specific cells. Follow up studies using this new model can provide valuable new insights in the immune cell-mediated pathogenesis of vascular disease. For example, current research in the pericyte field has demonstrated the involvement of pericytes in tissue fibrogenesis: upon activation by macrophage derived amphiregulin (an epidermal growth factor receptor (EGFR) ligand), pericytes transdifferentiate into myofibroblasts in a TGFβ dependent manner.[76] Yet, certain subtypes of pericytes, such as $CD73^+$ pericytes in the kidney, have been shown to suppress inflammation and prevent progressive renal fibrosis.[77] Furthermore, the presented model provides a suitable platform to allow in depth analysis of the contribution of different subtypes of pericytes in relation to inflammation control and fibrogenesis in multiple diseases including chronic kidney disease.

For diastolic heart failure, we have recently identified a possible role for the pericytes that support the cardiac microvascular bed in disease onset or progression. Characterized by increased stiffness in the left ventricle with decreased compliance and impaired relaxation, research of the pathogenesis of diastolic heart failure points towards a disease pathway with which involves endothelial dysfunction, vascular rarefaction, inflammation and fibrosis that negatively influences myocyte performance and promotes

cardiac wall stiffening. Most significantly, we have recently shown in a rat model of diastolic heart failure, that cardiac fibrosis initiates in microvascular foci, which are characterized by a disorganization of hyper proliferative endothelial cells and pericytes. These foci are hotbeds of inflammation and deposition of fibrosis-associated ECM components.[78] In addition, rise in TGFβ levels and TGFβ pathway activation plays a central role in pathogenesis of this disease. Despite these obvious links with inflammation and fibrosis, the role of pericytes has not been studied in diastolic heart failure.

Limitations of the study

In the current model, human brain-derived pericytes were used for mural cell support of the endothelial monolayer. Although human brain-derived pericytes are considered a specialized phenotype of perivascular cells, they are often used to conduct microvascular research.[21,79–82] Cross check with multiple GEO datasets of freshly isolated murine mural cells[82] with *in vitro* cultured iPSC derived pericytes[83] (GSE124579) and placental pericytes[84] (GSE117469) with our own dataset of *in vitro* brain derived pericytes showed many similarities.[85] Overlap of all genes with positive reads produces a list of 137 genes that includes prominent and well defined pericytes markers such as ACTA2, PDGFRB, NG2 (CSPG4), TAGLN, CD248, MYH11, DES, ZIC1 and MCAM.[85] The most prominent pericyte markers PDGFRB and NG2 were also expressed in the top tertile of the total RNA signal. These findings show that human brain-derived pericytes share a large number of common markers with pericytes derived from other sources.

The diameter of the current neovessels may be considered too large to mimic micro-vessels. One of the main aims of this study was to design and create a vessel-on-a-chip system that has the capacity to mimic circulating cell interaction with the vasculature *in vivo* during an inflammatory response. *In vivo*, leukocyte activation and subsequent rolling and adhesion to the vessel luminal surface mainly takes place in the post-capillary venules where shear rate and shear stress levels are intrinsically low.[86,88] These venules may range in 10–100 μm in diameter. In relation to this, pericytes are not only present in the capillaries, but also provide support to vessels with larger diameters, including pre- and post-arterioles, capillaries and venules (<100 μm) as reviewed in multiple publications.[33,89] Our present system supports neovessels with a diameter of 500 μm, which may be considered too large. For any vessel-on-a-chip system that focusses on faithfully recreating native biomechanical conditions, it remains very challenging to create vessels in the capillary range that can sustain prolonged physiologically relevant flow without damaging the integrity of the vessel structure or compromising on the stiffness of the supporting ECM or hydrogel. Thus far, several studies have reported the use of fully soft material encased channels with a diameter ranging between 360 and 800 μm, which permit perfusion.[15,16,30,90] Similar to our system, these previously reported setups were limited in their ability to further reduce the diameter to the desired range due to limitations in the biomechanical properties of the encasing ECM or hydrogel. Studies that have achieved flowed channels within the capillary range have their own disadvantages as most of the time, they can only sustain perfusion using low levels (bi-directional and non-continuous) of gravitational flow without the active control of mechanical pump systems.[41–43] Despite the discrepancy in size between venules and the neovessels in our current system, many traits in the natural behavior of pericytes and ECs during their interaction, such as pericyte recruitment and effect on the establishment of the endothelial barrier, could still be successfully demonstrated in our platform.

Channel size reduction may be achieved in future studies using the top-down subtractive 3D printing strategy, based on printing the predefined channels with a soluble material, such as carbohydrate glass[87] and Pluronic F127[31] before casting or 3D printing the hydrogel, followed by channel creation by dissolving the sacrificial materials. This approach allows creation of channels in a range of 1000 to 50 μm, although perfusion with physiological flow without disruption of the hydrogel wall will still remain an issue. Relatively high circumferential stretch (>110%) as a result of flow may cause channel expansion and disruption of cell–cell junctions in the endothelium thus compromising barrier function and vessel integrity. In the living body, the native micro-vessels are surrounded by tissue cells that provide additional mechanical support. An increase in hydrogel strength, so stretch remain limited under physiological flow levels, may provide the answer to gel encapsulated systems like ours. However, it has to be taken into consideration that the desired properties of an optimal hydrogel for the perfused vascular system require a delicate balance between what is supportive of biological function (such as maintaining migratory ability of mural cells through the hydrogel for self-organization) and providing mechanical strength and elasticity to counter act the circumferential stretch.

When considering the microvasculature, the shear stress level of 0.286 dyne per cm^2 is low compared to the levels reported by *e.g.* Koutsiaris *et al.* who calculated wall shear stress in the human eye.[86] Based on the diameter of the smallest human conjunctival capillaries, the wall shear stress was ~95 dyne per cm^2, whereas 2.8 dyne per cm^2 was calculated for the post-capillary venules.[86] Shear stress levels differ largely between organs and tissues and also varies considerably within the same tissue depending on the location in the capillary bed.[91] For example, the shear stress in glomerular capillaries ranges between 1 and 95 dyne per cm^2,[92] whereas shear stress in the capillaries of the highly vascularized placenta is calculated to be ~0.5 dyne per cm^2.[93] Furthermore, shear stress is often calculated based on the following equation: $\tau_w = 4\mu Q/\pi r3$, in which shear stress at the luminal wall (τ_w) depends on flow rate (Q), fluid viscosity (μ),

and inner radius the vessel (r). It has been suggested that although this is a correct assumption for larger straight vessels segments with limited bifurcations, an alternative formula should be used to calculated wall shear stress in capillaries of the microvascular bed: $\tau_w = \Delta Pd/4L$, with wall shear stress (τ_w) calculated from the pressure difference across the capillary (ΔP), and the inner diameter (d) and length (L) of the capillary.[94] By using this method for wall shear stress calculations, Cho *et al.* calculated that in murine mesentery capillaries, based on the pressure gradients reported,[95] wall shear stress in a micro-vessel was 0.16 dyne per cm^2.[94] Our calculated wall shear stress (0.286 dyne per cm^2) is similar compared to the study of Osaki *et al.*[16] Systems that use unmonitored gravitational flow have severely limited control over flow speed, as it will decline with exhaustion of the source reservoir, and are therefore unsuitable for studies with circulating cells which require controlled unidirectional flow with a consistent flow rate.[15,43,49] Some *in vitro* systems use Ibidi slides and pumps or other designs to perfuse immune cells in a blood vessel mimicking environment. In these systems, slide seeded ECs are perfused with neutrophils or other circulating cells with a shear stress between 0.5 and 1 dyne per cm^2.[11,65,69,96] These shear stress levels are close to the range of shear stress in our current microfluidic model.

Conclusions

In conclusion, we designed, fabricated and tested a novel vasculature microfluidic device to mimic complex vasculature tissue. Our vessel-on-a-chip can be easily produced and (live) monitored using a standard confocal microscope setup. This model enables the co-culture of multiple (vascular) cell types in a 3D ECM environment while being perfused with relevant microvascular flow levels. The high flexibility of this model allows researchers to study specific interactions between different cell types and cell–ECM interaction, in a background of different stimuli to mimic specific (disease) environments. Our current microfluidic device provides a unique tool to conduct *in vitro* analysis of the human microvasculature during the inflammation process of a multitude of different relevant human diseases.

Author contributions

Methodology: C. G. M. V. D., E. F. G. A. H., R. L. and C. C. Conceptualization: C. G. M. V. D., M. M. B., L. L. M., J. P., M. M. K., B. W. M. V. B., P. D. G., D. J. D., M. C. V., R. L. and C. C. Data curation: C. G. M. V. D, N. P., J. A., M. V. D. M. and L. K. Formal analysis: C. G. M. V. D. and C. C. Writing-original draft: C. G. M. V. D and C. C. Writing-review and editing: C. G. M. V. D., P. D. G., D. J. D., M. C. V., R. L. and C. C.

Conflicts of interest

There are no conflicts to declare.

Acknowledgements

We would like to thank Dr. O. G. de Jong for donating lentiviral GFP and dsRED constructs. This work was supported by Netherlands Foundation for Cardiovascular Excellence [C. C.], Netherlands Organization for Scientific Research Vidi grant [no. 91714302 to C. C.] and Material Driven Regeneration Consortium [Gravitation program to C. C., M. V.], the Erasmus MC fellowship grant [C. C.], the Regenerative Medicine Fellowship grant of the University Medical Center Utrecht [C. C.], and the Netherlands Cardiovascular Research Initiative: an initiative with support of the Dutch Heart Foundation [CVON2014-11 RECONNECT to C. C., D. D., and M. V.].

References

1 W. G. Chang and L. E. Niklason, *npj Regener. Med.*, 2017, **2**, 7.
2 E. Dejana, F. Orsenigo and M. G. Lampugnani, *J. Cell Sci.*, 2008, **121**(Pt 13), 2115–2122.
3 O. Tornavaca, M. Chia, N. Dufton, L. O. Almagro, D. E. Conway, A. M. Randi, M. A. Schwartz, K. Matter and M. S. Balda, *J. Cell Biol.*, 2015, **208**(6), 821–838.
4 J. R. Allport, W. A. Muller and F. W. Luscinskas, *J. Cell Biol.*, 2000, **148**(1), 203–216.
5 D. Vestweber, *Nat. Rev. Immunol.*, 2015, **15**(11), 692–704.
6 M. Schnoor, P. Alcaide, M. B. Voisin and J. D. van Buul, *Mediators Inflammation*, 2015, **2015**, 946509.
7 M. Leick, V. Azcutia, G. Newton and F. W. Luscinskas, *Cell Tissue Res.*, 2014, **355**(3), 647–656.
8 M. Lawrence, L. McIntire and S. Eskin, *Blood*, 1987, **70**(5), 1284–1290.
9 K. B. Abbitt and G. B. Nash, *Br. J. Haematol.*, 2001, **112**, 55–63.
10 R. Huang, W. Zheng, W. Liu, W. Zhang, Y. Long and X. Jiang, *Sci. Rep.*, 2015, **5**, 17768.
11 A. Ganguly, H. Zhang, R. Sharma, S. Parsons and K. D. Patel, *J. Visualized Exp.*, 2012(66), e4032.
12 M. Sato, N. Sasaki, M. Ato, S. Hirakawa, K. Sato and K. Sato, *PLoS One*, 2015, **10**(9), e0137301.
13 J. W. Song, S. P. Cavnar, A. C. Walker, K. E. Luker, M. Gupta, Y. C. Tung, G. D. Luker and S. Takayama, *PLoS One*, 2009, **4**(6), e5756.
14 H. Takahashi, K. Kato, K. Ueyama, M. Kobayashi, G. Baik, Y. Yukawa, J. I. Suehiro and Y. T. Matsunaga, *Sci. Rep.*, 2017, **7**, 42426.
15 D. H. Nguyen, S. C. Stapleton, M. T. Yang, S. S. Cha, C. K. Choi, P. A. Galie and C. S. Chen, *Proc. Natl. Acad. Sci. U. S. A.*, 2013, **110**(17), 6712–6717.
16 T. Osaki, T. Kakegawa, T. Kageyama, J. Enomoto, T. Nittami and J. Fukuda, *PLoS One*, 2015, **10**(4), e0123735.
17 M. Tehranirokh, A. Z. Kouzani, P. S. Francis and J. R. Kanwar, *Biomicrofluidics*, 2013, **7**(5), 51502.
18 K. H. Wong, J. M. Chan, R. D. Kamm and J. Tien, *Annu. Rev. Biomed. Eng.*, 2012, **14**, 205–230.
19 S. F. Lam, V. S. Shirure, Y. E. Chu, A. G. Soetikno and S. C. George, *PLoS One*, 2018, **13**(12), e0209574.

20 Y. Shin, S. H. Choi, E. Kim, E. Bylykbashi, J. A. Kim, S. Chung, D. Y. Kim, R. D. Kamm and R. E. Tanzi, *Adv. Sci.*, 2019, **6**(20), 1900962.
21 M. Campisi, Y. Shin, T. Osaki, C. Hajal, V. Chiono and R. D. Kamm, *Biomaterials*, 2018, **180**, 117–129.
22 S. Bang, S. R. Lee, J. Ko, K. Son, D. Tahk, J. Ahn, C. Im and N. L. Jeon, *Sci. Rep.*, 2017, **7**(1), 8083.
23 S. Lee, J. Ko, D. Park, S. R. Lee, M. Chung, Y. Lee and N. L. Jeon, *Lab Chip*, 2018, **18**(18), 2686–2709.
24 S. Kim, W. Kim, S. Lim and J. S. Jeon, *Bioengineering*, 2017, **4**(1), 8.
25 Y. K. Kurokawa, R. T. Yin, M. R. Shang, V. S. Shirure, M. L. Moya and S. C. George, *Tissue Eng., Part C*, 2017, **23**(8), 474–484.
26 K. Yamamoto, K. Tanimura, M. Watanabe, H. Sano, H. Uwamori, Y. Mabuchi, Y. Matsuzaki, S. Chung, R. D. Kamm, K. Tanishita and R. Sudo, *Tissue Eng., Part A*, 2019, **25**(5–6), 499–510.
27 T. Osaki, J. C. Serrano and R. D. Kamm, *Regener. Eng. Transl. Med.*, 2018, **4**(3), 120–132.
28 R. L. Thompson, E. A. Margolis, T. J. Ryan, B. J. Coisman, G. M. Price, K. H. K. Wong and J. Tien, *J. Biomed. Mater. Res., Part A*, 2018, **106**(1), 106–114.
29 N. Jusoh, J. Ko and N. L. Jeon, *APL Bioeng.*, 2019, **3**(3), 036101.
30 J. A. Kim, H. N. Kim, S. K. Im, S. Chung, J. Y. Kang and N. Choi, *Biomicrofluidics*, 2015, **9**(2), 024115.
31 D. B. Kolesky, R. L. Truby, A. S. Gladman, T. A. Busbee, K. A. Homan and J. A. Lewis, *Adv. Mater.*, 2014, **26**(19), 3124–3130.
32 A. Armulik, G. Genove and C. Betsholtz, *Dev. Cell*, 2011, **21**(2), 193–215.
33 C. G. van Dijk, F. E. Nieuweboer, J. Y. Pei, Y. J. Xu, P. Burgisser, E. van Mulligen, H. el Azzouzi, D. J. Duncker, M. C. Verhaar and C. Cheng, *Int. J. Cardiol.*, 2015, **190**, 75–89.
34 P. Lindahl, B. R. Johansson, P. Leveen and C. Betsholtz, *Science*, 1997, **277**(5323), 242–245.
35 E. A. Winkler, R. D. Bell and B. V. Zlokovic, *Mol. Neurodegener.*, 2010, **5**, 32.
36 M. Bjarnegard, M. Enge, J. Norlin, S. Gustafsdottir, S. Fredriksson, A. Abramsson, M. Takemoto, E. Gustafsson, R. Fassler and C. Betsholtz, *Development*, 2004, **131**(8), 1847–1857.
37 K. C. Chaw, M. Manimaran, E. H. Tay and S. Swaminathan, *Lab Chip*, 2007, **7**(8), 1041–1047.
38 Q. Zhang, T. Liu and J. Qin, *Lab Chip*, 2012, **12**(16), 2837–2842.
39 K. S. Kolahi, A. Donjacour, X. Liu, W. Lin, R. K. Simbulan, E. Bloise, E. Maltepe and P. Rinaudo, *PLoS One*, 2012, **7**(7), e41717.
40 H. Hassanisaber, L. Jafari, M. A. Campeau, O. Drevelle, M. A. Lauzon, E. Langelier, N. Faucheux and L. Rouleau, *Mater. Sci. Eng., C*, 2019, **98**, 572–583.
41 M. B. Chen, J. A. Whisler, J. Frose, C. Yu, Y. Shin and R. D. Kamm, *Nat. Protoc.*, 2017, **12**(5), 865–880.
42 S. Kim, M. Chung, J. Ahn, S. Lee and N. L. Jeon, *Lab Chip*, 2016, **16**(21), 4189–4199.
43 V. van Duinen, A. van den Heuvel, S. J. Trietsch, H. L. Lanz, J. M. van Gils, A. J. van Zonneveld, P. Vulto and T. Hankemeier, *Sci. Rep.*, 2017, **7**(1), 18071.
44 G. M. Price and J. Tien, *Biological Microarrays*, 2011, pp. 281–293.
45 G. Lamberti, B. Prabhakarpandian, C. Garson, A. Smith, K. Pant, B. Wang and M. F. Kiani, *Anal. Chem.*, 2014, **86**(16), 8344–8351.
46 M. B. Lawrence, G. S. Kansas, E. J. Kunkel and K. Ley, *J. Cell Biol.*, 1997, **137**(1), 261.
47 S. I. Simon, Y. Hu, D. Vestweber and C. W. Smith, *J. Immunol.*, 2000, **164**(8), 4348–4358.
48 I. K. Zervantonakis, S. K. Hughes-Alford, J. L. Charest, J. S. Condeelis, F. B. Gertler and R. D. Kamm, *Proc. Natl. Acad. Sci. U. S. A.*, 2012, **109**(34), 13515–13520.
49 Y. Zheng, J. Chen, M. Craven, N. W. Choi, S. Totorica, A. Diaz-Santana, P. Kermani, B. Hempstead, C. Fischbach-Teschl, J. A. Lopez and A. D. Stroock, *Proc. Natl. Acad. Sci. U. S. A.*, 2012, **109**(24), 9342–9347.
50 S. Kim, H. Lee, M. Chung and N. L. Jeon, *Lab Chip*, 2013, **13**(8), 1489–1500.
51 H. Lee, S. Kim, M. Chung, J. H. Kim and N. L. Jeon, *Microvasc. Res.*, 2014, **91**, 90–98.
52 J. Kim, M. Chung, S. Kim, D. H. Jo, J. H. Kim and N. L. Jeon, *PLoS One*, 2015, **10**(7), e0133880.
53 S. Alimperti, T. Mirabella, V. Bajaj, W. Polacheck, D. M. Pirone, J. Duffield, J. Eyckmans, R. K. Assoian and C. S. Chen, *Proc. Natl. Acad. Sci. U. S. A.*, 2017, **114**(33), 8758–8763.
54 S. Huveneers, J. Oldenburg, E. Spanjaard, G. van der Krogt, I. Grigoriev, A. Akhmanova, H. Rehmann and J. de Rooij, *J. Cell Biol.*, 2012, **196**(5), 641–652.
55 G. P. van Nieuw Amerongen, S. van Delft, M. A. Vermeer, J. G. Collard and V. W. van Hinsbergh, *Circ. Res.*, 2000, **87**(4), 335–340.
56 B. Wojciak-Stothard, S. Potempa, T. Eichholtz and A. J. Ridley, *J. Cell Sci.*, 2001, **114**(Pt 7), 1343–1355.
57 K. M. Chrobak, D. R. Potter and J. Tien, *Microvasc. Res.*, 2006, **71**(3), 185–196.
58 J. S. Choi, Y. J. Choi, S. H. Park, J. S. Kang and Y. H. Kang, *J. Nutr.*, 2004, **134**(5), 1013–1019.
59 M. H. Bosteen, K. Tritsaris, A. J. Hansen and S. Dissing, *Pflugers Arch.*, 2014, **466**(5), 961–972.
60 H. Zhang, Y. Park, J. Wu, X. Chen, S. Lee, J. Yang, K. C. Dellsperger and C. Zhang, *Clin. Sci.*, 2009, **116**(3), 219–230.
61 A. H. Sprague and R. A. Khalil, *Biochem. Pharmacol.*, 2009, **78**(6), 539–552.
62 M. T. Nakada, S. H. Tam, D. S. Woulfe, K. A. Casper, R. A. Swerlick and J. Ghrayeb, *Cell Adhes. Commun.*, 1998, **5**(6), 491–503.
63 P. R. Clark, T. D. Manes, J. S. Pober and M. S. Kluger, *J. Invest. Dermatol.*, 2007, **127**(4), 762–774.
64 T. Bian, H. Li, Q. Zhou, C. Ni, Y. Zhang and F. Yan, *Mediators Inflammation*, 2017, **2017**, 8529542.
65 R. Oberoi, J. Schuett, H. Schuett, A. K. Koch, M. Luchtefeld, K. Grote and B. Schieffer, *PLoS One*, 2016, **11**(7), e0160145.

66 S. Thilagar, R. Theyagarajan, U. Sudhakar, S. Suresh, P. Saketharaman and N. Ahamed, *J. Indian Soc. Periodontol.*, 2018, **22**(2), 116–121.
67 H. C. Pape, R. E. Schmidt, J. Rice, M. van Griensven, R. das Gupta, C. Krettek and H. Tscherne, *Crit. Care Med.*, 2000, **28**(10), 3441–3448.
68 S. Haider and M. Knofler, *Placenta*, 2009, **30**(2), 111–123.
69 H. Munir, G. E. Rainger, G. B. Nash and H. McGettrick, *J. Visualized Exp.*, 2015(95), e52480.
70 K. Stark, A. Eckart, S. Haidari, A. Tirniceriu, M. Lorenz, M. L. von Bruhl, F. Gartner, A. G. Khandoga, K. R. Legate, R. Pless, I. Hepper, K. Lauber, B. Walzog and S. Massberg, *Nat. Immunol.*, 2013, **14**(1), 41–51.
71 D. Proebstl, M. B. Voisin, A. Woodfin, J. Whiteford, F. D'Acquisto, G. E. Jones, D. Rowe and S. Nourshargh, *J. Exp. Med.*, 2012, **209**(6), 1219–1234.
72 C. E. Ayres-Sander, H. Lauridsen, C. L. Maier, P. Sava, J. S. Pober and A. L. Gonzalez, *PLoS One*, 2013, **8**(3), e60025.
73 A. Tan, K. Fujisawa, Y. Yukawa and Y. T. Matsunaga, *Biomater. Sci.*, 2016, **4**(10), 1503–1514.
74 W. Jia, P. S. Gungor-Ozkerim, Y. S. Zhang, K. Yue, K. Zhu, W. Liu, Q. Pi, B. Byambaa, M. R. Dokmeci, S. R. Shin and A. Khademhosseini, *Biomaterials*, 2016, **106**, 58–68.
75 I. Pepelanova, K. Kruppa, T. Scheper and A. Lavrentieva, *Bioengineering*, 2018, **5**(3), pii: E55.
76 C. M. Minutti, R. V. Modak, F. Macdonald, F. Li, D. J. Smyth, D. A. Dorward, N. Blair, C. Husovsky, A. Muir, E. Ciampazolias, R. Dobie, R. M. Maizels, T. J. Kendall, D. W. Griggs, M. Kopf, N. C. Henderson and D. M. Zaiss, *Immunity*, 2019, **50**, 645–654.
77 H. M. Perry, N. Görldt, S. J. Sung, L. Huang, K. P. Rudnicka, I. M. Encamacion, A. Bajwa, S. Tanaka, N. Poudel, J. Yao, D. L. Rosin, J. Schrader and M. D. Okusa, *Am. J. Physiol. Renal Physiol.*, 2019, **317**, F658–F669.
78 C. G. M. van Dijk, N. R. Oosterhuis, Y. J. Xu, M. M. Brandt, W. J. Paulus, L. van Heerebeek, D. J. Duncker, M. C. Verhaar, D. Fontoura, A. P. Lourenco, A. F. Leite-Moreira, I. Falcão-Pires, J. A. Joles and C. Cheng, *Circ.: Heart Failure*, 2016, **9**(4), e002760.
79 M. M. Brandt, C. G. M. van Dijk, I. Chrifi, H. M. Kool, P. E. Bürgisser, L. Louzao-Martinez, J. Pei, R. J. Rottier, M. C. Verhaar, D. J. Duncker and C. Cheng, *Angiogenesis*, 2018, **21**(4), 805–821.
80 I. Chrifi, L. Louzao-Martinez, M. M. Brandt, C. G. M. van Dijk, P. E. Bürgisser, C. Zhu, J. M. Kros, M. C. Verhaar, D. J. Duncker and C. Cheng, *Angiogenesis*, 2018, **22**(1), 75–93.
81 M. Vanlandewijck, T. Lebouvier, M. Andaloussi Mäe, K. Nahar, S. Hornemann, D. Kenkel, S. I. Cunha, J. Lennartsson, A. Boss, C.-H. Heldin, A. Keller and C. Betsholtz, *PLoS One*, 2015, **10**(11), e0143407.
82 L. He, M. Vanlandewijck, E. Raschperger, M. Andaloussi Mäe, B. Jung, T. Lebouvier, K. Ando, J. Hofmann, A. Keller and C. Betsholtz, *Sci. Rep.*, 2016, **6**, 35108.
83 M. J. Stebbins, B. D. Gastfriend, S. G. Canfield, M.-S. Lee, D. Richards, M. G. Faubion, W.-J. Li, R. Daneman, S. P. Palecek and E. V. Shusta, *Sci. Adv.*, 2019, **5**(3), eaau7375.
84 R. A. Wimmer, A. Leopoldi, M. Aichinger, N. Wick, B. Hantusch, M. Novatchkova, J. Taubenschmid, M. Hämmerkle, C. Esk, J. A. Bagley, D. Lindenhofer, G. Chen, M. Boehm, C. A. Agu, F. Yang, B. Fu, J. Zuber, J. A. Knoblich, D. Kerjaschki and J. M. Penninger, *Nature*, 2019, **565**, 505–510.
85 M. M. Brandt, C. G. M. van Dijk, R. Maringanti, I. Chrifi, R. Kramann, M. C. Verhaar, D. J. Duncker, M. Mokry and C. Cheng, *Sci. Rep.*, 2019, **9**(1), 15586.
86 A. G. Koutsiaris, S. V. Tachmitzi, N. Batis, M. G. Kotoula, C. H. Karabatsas, E. Tsironi and D. Z. Chatzoulis, *Biorheology*, 2007, **44**, 375–386.
87 J. S. Miller, K. R. Stevens, M. T. Yang, B. M. Baker, D. H. T. Nguyen, C. M. Cohen, E. Toro, A. A. Chen, P. A. Galie, X. Yu, R. Chaturvedi, S. N. Bhatia and C. S. Chen, *Nat. Mater.*, 2012, **11**, 768–774.
88 J. P. Girard and T. A. Springer, *Immunol. Today*, 1995, **16**(9), 449–457.
89 L. Díaz-Flores, R. Gutiérrez, J. F. Madrid, H. Varela, F. Valladares, E. Acosta, P. Martín-Vasallo and L. Díaz-Flores Jr., *Histol. Histopathol.*, 2009, **24**, 909–969.
90 A. Herland, A. D. van der Meer, E. A. FitzGerald, T. E. Park, J. J. Sleeboom and D. E. Ingber, *PLoS One*, 2016, **11**(3), e0150360.
91 C. Cheng, F. Helderman, D. Tempel, D. Segers, B. Hierck, R. Poelmann, A. van Tol, D. J. Duncker, D. Robbers-Visser, N. T. Ursem, R. van Haperen, J. J. Wentzel, F. Gijsen, A. F. van der Steen, R. de Crom and R. Krams, *Atherosclerosis*, 2007, **195**(2), 225–235.
92 B. J. Ballermann, A. Dardik, E. Eng and A. Liu, *Kidney Int. Suppl.*, 1998, **67**, S100–S108.
93 W. M. Tun, C. H. Yap, S. N. Saw, J. L. James and A. R. Clark, *Sci. Rep.*, 2019, **9**(1), 9876.
94 Y. I. Cho and D. J. Cho, *Korean Circ. J.*, 2011, **41**(6), 287–295.
95 A. R. Pries, T. W. Secomb and P. Gaehtgens, *Am. J. Physiol.*, 1995, **269**(5), H1713–H1722.
96 S. K. Shaw, S. Ma, M. B. Kim, R. M. Rao, C. U. Hartman, R. M. Froio, L. Yang, T. Jones, Y. Liu, A. Nusrat, C. A. Parkos and F. W. Luscinskas, *J. Exp. Med.*, 2004, **200**(12), 1571–1580.